Agility of spin Hall nano-oscillators

Trindade Goncalves, F. J.; Hache, T.; Bejarano, M.; Hula, T.; Hellwig, O.; Faßbender, J.; Schultheiß, H.;

Originally published:

November 2021

Physical Review Applied 16(2021)5, 054050

DOI: https://doi.org/10.1103/PhysRevApplied.16.054050

Agility of spin Hall nano-oscillators

F. J. T. Gonçalves,[1] T. Hache,[1,2] M. Bejarano,[1,2] T. Hula,[1,2] O. Hellwig,[1,2] J. Fassbender,[1,3] and H. Schultheiss[1,3]

[1] *Helmholtz-Zentrum Dresden–Rossendorf, Institute of Ion Beam Physics and Materials Research, Bautzner Landstraße 400, 01328 Dresden, Germany*

[2] *Institut für Physik, Technische Universität Chemnitz, 09107 Chemnitz, Germany*

[3] *Technische Universität Dresden, 01062 Dresden, Germany*

We investigate the temporal response of constriction-based spin Hall nano-oscillators driven by pulsed stimuli using time-resolved Brillouin light scattering microscopy. Magnetization auto-oscillations, enabled by spin Hall effect and spin orbit torque, can be obtained using input voltage pulses of a few nanoseconds in duration. The combination of voltage and microwave pulses allows to generate auto-oscillation signals with multi-level amplitude and frequency in the time-domain. Our findings suggest that the lead time of processes such as synchronization and logic using spin Hall nano-oscillators can be reduced to the nanosecond time-scale.

I. INTRODUCTION

Magnetic oscillators are among the most promising means to perform brain inspired solid-state based computation [1, 2]. These are primarily based on magnetization auto-oscillations (AOs) in the gigahertz frequency range. AOs arise when the Gilbert damping is compensated by the torque transferred from a pure spin or spin polarised current to the magnetization, due to spin orbit torque (SOT) or spin transfer torque [3–7]. Here, the pure spin current is generated via spin Hall effect [8, 9], in an adjacent non-ferromagnetic, metallic layer with large spin Hall angle [10–12]. Over the recent years, two main prototypical oscillator geometries have surfaced: the spin Hall nano-oscillators (SHNO) [13–15] and the spin torque nano-oscillators [16, 17]. Often, these are physically arrayed into a network, when synchronisation between oscillators [18–20] allows for complex operations, such as pattern recognition [21, 22]. To some extent, an isolated magnetic oscillator in itself can mimic a pseudo-network of oscillators [23, 24] if external time-dependent stimuli are applied to exploit its nonlinear response. Thus, an important requisite for a magnetic oscillator is agility, that is, the ability to respond to time-dependent external stimuli in a way that the resulting amplitude, frequency or phase can be utilized reliably as a processing output.

In this manuscript, we investigate the temporal response of SHNOs driven by voltage pulses (V_p) and microwave pulses (RF_p). We found that AO signals can be generated using few-nanosecond wide voltage pulses. We discuss how the AO response can be improved by means of injection-locking to an external microwave pulse. Furthermore, we demonstrate how the pulsed operation results in a reliable multi-level AO amplitude and frequency in the time-domain.

II. SHNO GEOMETRY AND METHODS

Figure 1(a) shows a top-view scanning electron microscopy (SEM) image of the SHNO. The two magnetic disks have a radius of 2.6 µm and overlap by approximately 50 nm, resulting in a constriction width of 1.13 µm. The structures were fabricated on a silicon substrate using a resist mask created by electron-beam-lithography (EBL), followed by sputtering of the thin film layers Ta(2 nm)/Pt(7 nm)/$Ni_{81}Fe_{19}$(5 nm)/Ta(2 nm) and lift-off. The electrical contacts were created using an additional EBL resist mask followed by thermal evaporation of the metals (Cr/Au) and lift-off. The structure under test has an average resistance 350 Ω.

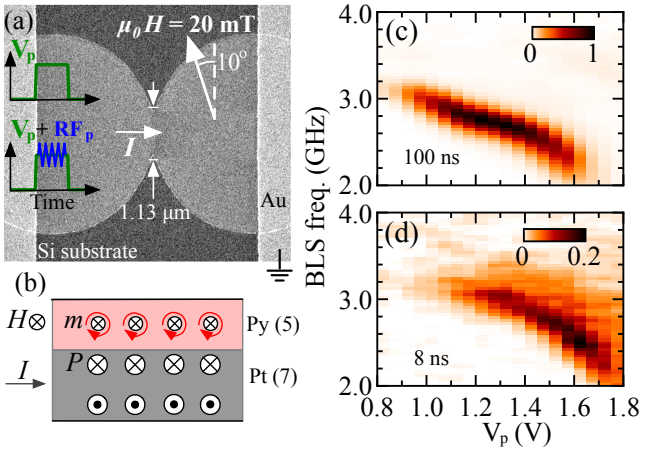

FIG. 1 (Color online). (a) SEM image of the SHNO and measurement geometry. (b) Schematic illustration of the layer stack, highlighting the direction of the current (I), the polarisation of the pure spin current (P) and the precession induced on the magnetic moment (m) of the Py ($Ni_{81}Fe_{19}$) layer. (c)-(d) BLS spectra for voltage pulses with durations of (c) 100 ns and (d) 8 ns.

The temporal response of the SHNOs was tested under two types of pulse excitations, as illustrated in Fig. 1(a). The first type concerned the use of voltage pulses (V_p) to drive the AOs and the second type concerned the combined use of voltage and microwave pulses (RF_p) in order to induce injection-locking of the AOs to the external RF stimuli.

Figures 1(a)-(b) highlight the magnetic field and current directions necessary for generating AOs by means

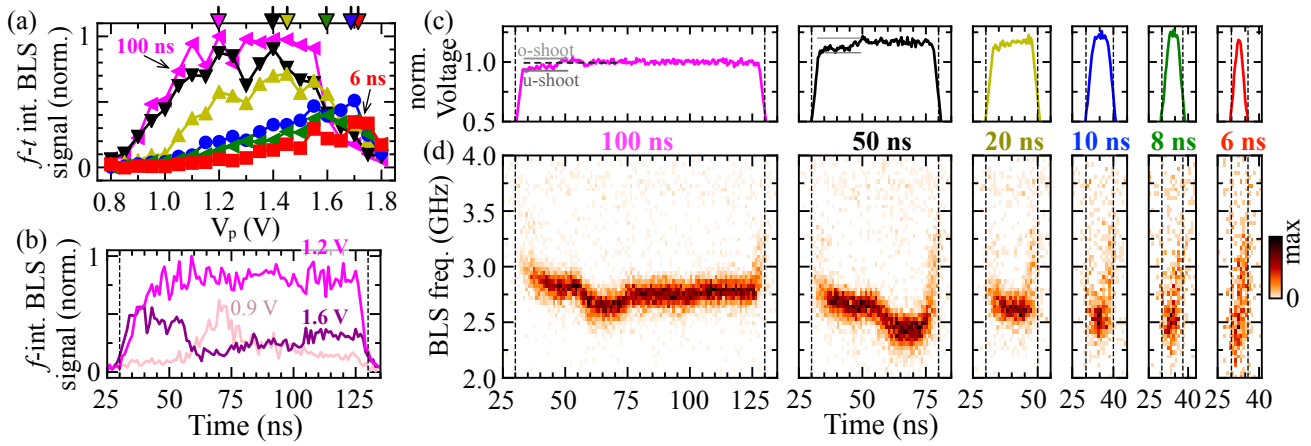

FIG. 2 (Color online). (a) Frequency-and-time integrated BLS signal plotted as a function of V_p, for the various pulse durations. Signal integrated between 1.8 GHz and 7.1 GHz, over the pulse width and normalised with respect to the signal obtained using 100 ns pulses. (b) Frequency-integrated TR-BLS data obtained using 100 ns wide pulses, for V_p values of 0.9 V, 1.2 V(V_{op}), and 1.6 V. Vertical dashed lines are coincident with the onset and outset of the AOs (same for (d)). (c) Time dependence of V_p, measured using an oscilloscope and normalised with respect to V_{op} = 1.2 V. (left panel) (u)under-shoot and (o)over-shoot highlight the variations of the instantaneous voltage with respect to V_p. (d) TR-BLS spectra obtained at V_{op}, for the different pulse durations. The values of V_{op} are indicated in (a) by the vertical arrows. From left to right, the maximum of the intensity-coded scale-bars have the values of 1, 0.8, 0.8, 0.4, 0.3 and 0.2, respectively.

of SHE and SOT [3, 4, 10]. In particular, the direction of the injected current (I), the polarisation of the pure spin current (P) arising due to SHE and the direction of the magnetic moment (m) in the presence of an in-plane magnetic field (H). The external magnetic field must be applied in the direction perpendicular to the current flow, as the SOT efficiency is maximised [5, 10, 13]. At sufficiently large current densities, this leads to damping compensation and consequent emergence of AOs in the constriction region. In the present experiments, H is tilted by 80 degrees with regard to I, so that the field-like torque induced by the microwave current in the Pt layer, has a component orthogonal to m. This results in an increased coupling between the AOs and the external microwave field, with little impact on the AOs [25, 26]. In all experiments reported, the magnitude of H was first increased to 200 mT for the purpose of saturating the magnetization, and then decreased to 20 mT.

Time-resolved Brillouin light scattering microscopy (TR-BLS) was employed to measure the frequency spectra of the AOs as a function of time. Using this stroboscopic technique, nanosecond time resolution and sub-micron spatial resolution can be achieved [27]. The measurement apparatus included electrical inputs for injecting voltage pulses and RF signals, generated by an arbitrary waveform generator and microwave source, combined via a microwave diplexer. The voltage pulses have a trapezoidal shape, with rise and fall time of 4 ns and a repetition rate of 4 MHz.

III. MAGNETIZATION AUTO-OSCILLATIONS DRIVEN BY VOLTAGE PULSES

Figures 1(c)-(d) show the BLS spectra as a function of V_p, obtained using pulses with durations of 100 ns and 8 ns, respectively. This data representation provides an overview of the frequency and intensity of the generated AOs. Despite the difference between the BLS intensity obtained using 100 ns and 8 ns voltage pulses, both spectra exhibit a similar trend, where the frequency of the AO mode observed varied from 3 GHz to 2.2 GHz with increasing V_p. Such frequency downshift is consistent with theory and with previous experiments involving SHNOs with a similar geometry [5, 13]. Note that in the BLS data obtained with the 100 ns pulses, the maximum intensity is obtained at V_p = 1.2 V while the BLS data obtained with the 8 ns pulses exhibited a maximum intensity at V_p = 1.6 V. Importantly, we provide first hand-demonstration that AOs can be obtained using few-nanosecond wide voltage pulses.

Figure 2(a) shows a summary of the frequency- and time-integrated BLS intensity, as a function of V_p and pulse width. The voltages that resulted in the maximum integrated AO amplitude were designated as optimal voltages V_{op} and are indicated by the vertical arrows. Here, we find that V_{op} increases from 1.2 V to 1.7 V with decreasing the pulse width from 100 ns to 6 ns. The integrated AO signal obtained using 100 ns and 50 ns wide pulses, shows a similar maximum amplitude. The 20 ns wide pulses resulted in a 25 % reduction of the maximum amplitude, while the 6 ns pulses resulted in a 65 % decrease of the integrated AO amplitude.

Figure 2(b) shows the time dependence of the frequency-integrated BLS signal obtained using 100 ns wide voltage pulses, for three different values of V_p. We found that the trapezoidal time-dependence of the input voltage was best converted to the time-dependence of the AO signal when V_{op} was applied. If the nominal input voltage was either below or above V_{op}, the amplitude of the AOs was not distributed evenly within the pulse width, as exemplified by the AO signal obtained for V_p values of 0.9 V and 1.6 V.

The time dependence of the voltage signals applied to the SHNO, measured using an oscilloscope, are shown in Fig. 2(c). Note that the initial segment of the voltage signal exhibits an undershoot and an overshoot of 6 % and 4 %, respectively, as highlighted by the horizontal dashed lines for the case of the 100 ns wide pulse, but it can also be observed in the 50 ns pulse. Such behaviour is reminiscent of the ringing effect in the RLC-equivalent circuit formed by the electrical cables, the electrical contacts on the substrate and the SHNO, as response to sudden changes in the input signal.

TR-BLS spectra, resulting from applying the voltage pulses, are shown in Fig. 2(d) at the indicated pulse widths, obtained at the corresponding V_{op} values. In general, we find that AO signal is detected for values of the instantaneous voltage above 50 % of V_{op}. This correspondence is highlighted by the vertical dashed lines at the onset and outset of the AO signals and voltage pulses.

For 100 ns wide pulses (shown on the leftmost panel in Fig. 2(d)) we observe that in the early stages of the voltage pulse, between 35 ns and 70 ns, the AO frequency varies from 2.95 GHz to 2.65 GHz, followed by an increase to 2.80 GHz at 75 ns. The frequency oscillations in the AO signal are caused by oscillations in the instantaneous voltage (current), as discussed above. From the data shown in Fig. 1(c), we note that a variation of 6 % around V_{op} can cause shifts in the AO frequency of about 200 MHz, consistent with the frequency oscillations shown in Fig. 2(d) [28]. When $t > 75$ ns, the AO frequency stabilizes at 2.80 GHz, as the voltage signal appears to reach a steady state. At the same time, the frequency linewidth of the signal reaches a minimum of 150 MHz. We note that this value is not the real AO linewidth but rather the result of broadening due to the TR-BLS detection method [29]. When approaching the outset of the AO signal, we observe an upshift of the AO frequency, simultaneously with a decrease of the amplitude, coincident with the sharp decrease in the voltage at the pulse outset. The sudden frequency upshift is in agreement with the results shown in Figs. 1(c)-(d), where for smaller nominal voltages, we obtain larger AO frequencies and smaller amplitudes.

The TR-BLS data obtained using shorter pulses shows a behaviour similar to that described for the 100 ns pulses, particularly, the variation of the AO frequency that follows the pulse onset and the steep frequency upshift at the pulse outset. A noticeable difference is the decrease in the AO frequency with decreasing pulse width, which is explained by the increasingly larger values of V_{OP}, as discussed with Fig. 2(a). In the limit of the shortest voltage pulses, one is unable to reach large AO amplitude as shown by the 60 % reduction in the integrated BLS signal, compared to that obtained with 100 ns pulses. We also note that the use of short pulses comes with the disadvantage of having a spreading of the AO frequency over the short existence of the pulse due to the rise and fall time of the pulses.

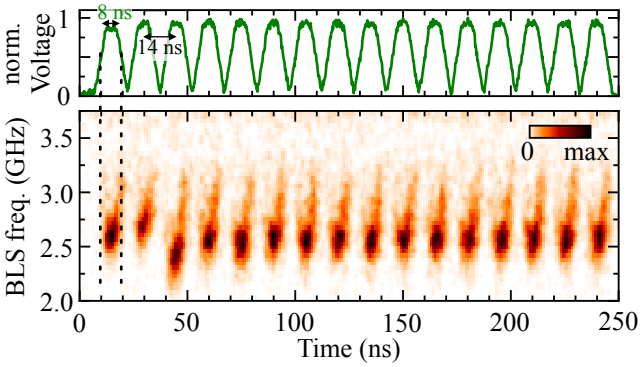

FIG. 3 (Color online). (a) (top) Time dependence of the voltage pulse train ($V_p = 1.1$ V), measured using an oscilloscope, and (bottom) resulting TR-BLS spectra.

An advantage of the fast AO response is the possibility to generate a train of closely spaced AO pulses in the time-domain. This functionality is demonstrated in Fig. 3, where we show the TR-BLS spectra generated by a train of 8 ns voltage pulses with $V_p = 1.1$ V and a period of 14 ns. It can be seen that the short bursts of AO signal can be repeated reliably over large time-scales. Next, we discuss the agility of SHNOs when in the presence of high frequency stimuli, particularly, the case where microwave pulses are utilised as a frequency-lock to the AO signal generated by voltage pulses.

IV. INJECTION-LOCKING USING MICROWAVE PULSES

In conventional injection-locking experiments, a magnetic field and a direct current are applied to the SHNO together with the external continuous wave (CW) RF signal that couples to the AOs [25, 30, 31]. If the frequency of the RF signal, f, is close to either the natural AO frequency, f_{AO}, or $2f_{AO}$, the external RF stimuli pulls the AO frequency toward its own frequency (or $f/2$). This effect is observed over a range of frequencies surrounding f_{AO}, namely the injection-locking range, which can reach several hundreds of megahertz, depending on parameters such as magnetic field strength, applied direct current and microwave power [25, 30, 31]. Injection-locking is also known to result in a larger AO amplitude [26, 32, 33].

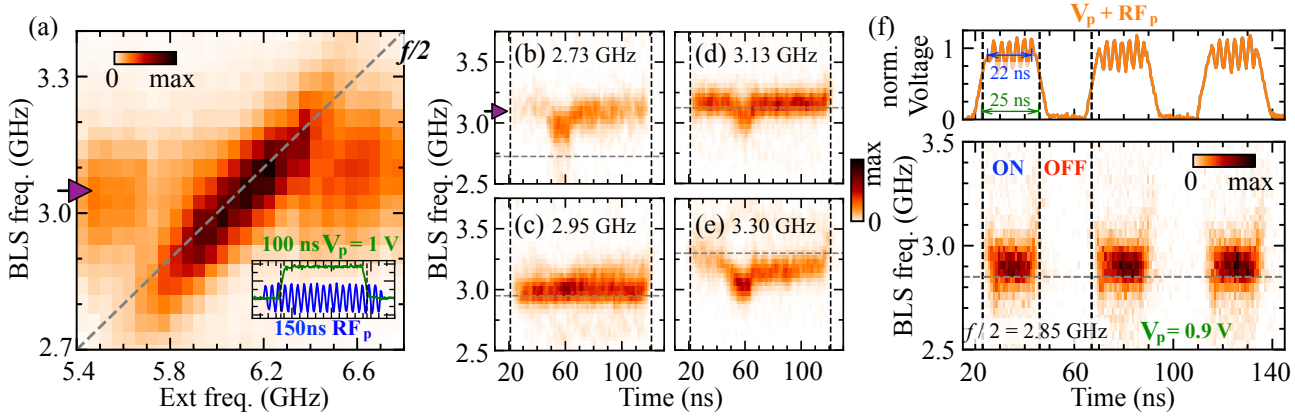

FIG. 4 (Color online). (a) BLS spectra as a function of the external RF frequency (f) obtained using of 150 ns wide RF pulses (at t = 0 ns), followed by a 100 ns wide voltage pulse (at t = 25 ns), as shown in the inset plot (RF power 1 dBm). The diagonal line indicates the values of $f/2$. The arrow in magenta indicates f_{AO} (same as in (b)). (b)-(e) TR-BLS spectra at the $f/2$ values of RF_p, indicated also by the horizontal dashed lines. The vertical dashed-lines indicate the onset and outset of the voltage pulse. The colour-coded intensity was normalised to a common value. (f) (top) Time-dependence of the input voltage of V_p+RF_p, and (bottom) resulting TR-BLS spectra (RF power 1 dBm).

In the present manuscript, we created the conditions for injection-locking to occur, except that instead of the direct current and CW RF signals we applied voltage and RF pulses. The BLS data, shown in Fig. 4(a), was obtained while applying 150 ns wide RF pulses to the SHNO (at t = 0 ns) combined with 100 ns wide voltage pulses applied (at t = 25 ns). The inset plot shows the time-dependence of the applied voltage and the RF pulse (RF_p). The nominal voltage, V_p was set to 1 V, and the frequency (f) of the RF pulses was varied from 5.4 GHz to 6.8 GHz ($f \sim 2f_{AO}$) with a constant nominal RF power of 1 dBm. Compared to the injection-locking obtained when $f \sim f_{AO}$, the frequency regime of $f \sim 2f_{AO}$, exhibited a wider frequency locking range and larger AO amplitudes, so only this case is discussed.

In Fig. 4(a), the frequencies corresponding to $f/2$ are illustrated by the diagonal dashed-line. For values of $f/2$ well below 2.85 GHz, the frequency of the AO signal is constant, at f_{AO}. When $f/2\sim$ 2.9 GHz, we observe a down-shift of the AO frequency simultaneously with an increase in the AO amplitude. Large amplitude AOs prevail as $f/2$ increases to 3.25 GHz. Above this frequency value, the AO amplitude decreases, and f_{AO} is gradually recovered. In these measurements, we obtained a frequency locking range of approximately 350 MHz.

Figures 4(b)-(e) show the TR-BLS spectra obtained at the indicated $f/2$ values of RF_p. An example of the AO signal in the limit of $f/2 << f_{AO}$ is shown in Fig. 4(b). The spectra exhibits a weak AO mode at $f \sim$ 3.0 GHz, whose amplitude is not evenly distributed within the duration of the voltage pulse. The time-varying AO amplitude seen here is consistent with the results discussed in Fig. 2(b).

Figures 4(c)-(d) show the TR-BLS spectra obtained for $f/2$ values within the frequency locking range, as seen in Fig. 4(a)). When $f/2$ = 2.95 GHz, not only we obtain an overall larger AO amplitude, but we also observe that the AO frequency and amplitude remains nearly constant within the duration of the voltage pulse. In the case where $f/2$ = 3.13 GHz, despite the large BLS signal, some oscillations in the AO frequency reappear at $t \sim$ 60 ns, as a result of a reduced injection-locking efficiency. In the example shown in Fig. 4(e), where $f/2 >> f_{AO}$, the injection-locking efficiency is again low, as the time dependence of the natural AO mode is partially restored, at 3.04 GHz.

When comparing the results shown in Figs. 4(b),(e) with those shown in Figs. 4(c),(d), we note that, when $f/2 \simeq f_{AO}$, the amplitude of the AOs is more evenly distributed throughout the duration of the voltage pulse. Despite the voltage oscillations inherent to the ringing effect of the input circuit, the AO signal remains stable within the pulse duration, demonstrating that improvements in the agility of the SHNO are achieved by means of injection-locking.

Injection-locking allowed us to achieve pulsed AO signals with a comparably large amplitude, in addition to the frequency tunability within the locking-range. This is further demonstrated in Fig. 4(f), where the TR-BLS data shown were obtained using voltage and RF pulses with similar duration and periodicity. In this case, 25 ns wide voltage pulses were combined with 22 ns wide RF pulses. The frequency of the RF pulses shown here is within the frequency locking range of the measured device. The resulting TR-BLS spectra shows a well defined intensity in the time-domain. From an application standpoint, the time segments with well defined amplitude levels may be interpreted as output levels ON/OFF or '1'/'0'.

The results discussed so far suggest that the interplay

between voltage and RF pulses gives rise to multi-level time-domain amplitude patterns. In Fig. 5 we demonstrate two ways in which the voltage and RF inputs can be combined in order to generate short-time segments with well defined levels of AO amplitude.

In the method discussed with Figs. 5(a)-(e), voltage pulses with a duration of 125 ns ($V_p = 1$ V) were applied to the SHNO. Following the onset of the AO signal, we applied a sequence of three RF pulses, with 28 ns width and a separation of 15 ns. The time dependence of the input stimuli is shown in Fig. 5(a), where the vertical dashed lines coincide with the onset and outset of each RF pulse. Figure 5(b) shows the TR-BLS spectra of the natural AO mode, obtained with the RF pulses switched off. Here, the oscillations in the AO frequency and the uneven distribution of the AO amplitude in the time-domain are consistent with the ringing behaviour of the AO signal, discussed with Fig. 2 (c).

The TR-BLS spectra of the pulsed injection-locking sequence are shown in Figs. 5(c)-(d), for $f/2$ values of 2.9 GHz and 3.05 GHz, respectively, chosen within the frequency locking range of the measured device. As expected, injection-locking occurs only during the three time segments coincident with the RF pulses. For the other two segments, where the RF excitation is switched off, the AO amplitude is reduced considerably as the natural AO frequency is restored.

Figure 5(e) shows the BLS signals integrated between 2.6 GHz and 3.5 GHz, obtained from the data shown in Figs. 5(b)-(d). The frequency range of the integration (df) is illustrated by the horizontal lines. First, note that by applying the first RF pulse immediately after the onset of the AOs, the instantaneous amplitude increased such that the time-profile of the AO amplitude became similar to that of the input voltage pulse (Fig. 5(a)). The two RF pulses that followed resulted in twice the AO amplitude compared to the natural AO mode. Using this approach, we obtain an amplitude modulated AO signal, reminiscent of a two-level system alternating between the frequency-locked state (1) and the natural AO state (0.5).

Next, we discuss a method which allows us to obtain amplitude modulation of two frequencies at distinct time segments of a voltage pulse train. The voltage of the trapezoidal pulse varies between 1 V and 0.5 V, as shown in Fig. 5(f). Here, the line in green corresponds to the trapezoidal pulses with a duration of 12 ns and a period of 30 ns, while the line in orange shows the voltage pulses combined with a CW RF signal.

The TR-BLS spectra obtained when applying the voltage pulses only (RF_p is off) is shown in Fig. 5(g), where we note that the AO mode appears at 2.95 GHz, in the time segments where the instantaneous voltage is equal to V_p. Here, the frequency upshift observed at the onset and outset of the AO signal is coincident with the time segments corresponding to the rise and fall of the voltage pulses. In the time segments coincident with $V_p/2 = 0.5$ V, the AO signal was too small to be detected, as expected from the results presented in Fig. 1(c).

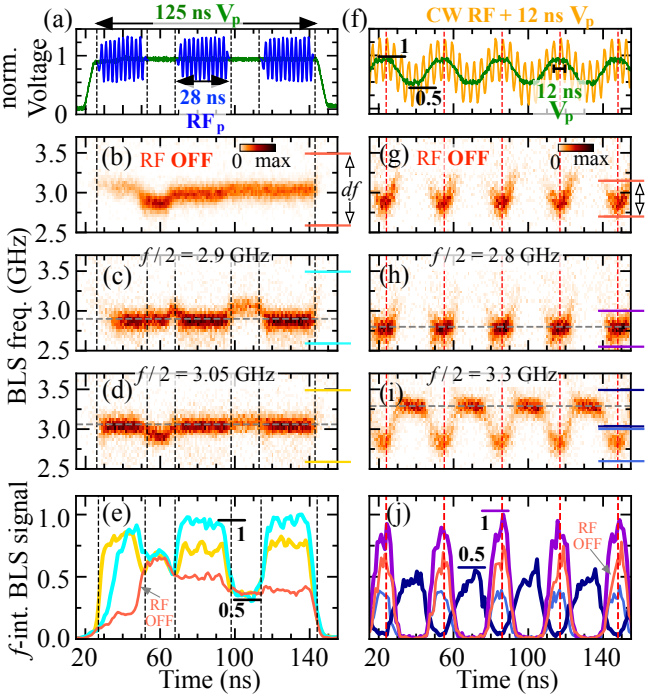

FIG. 5 (Color online). (a) Time dependence of V_p (green) and the RF pulses (blue). (b) TR-BLS spectra measured while applying $V_p = 1$ V only (RF_p off). (c)-(d) TR-BLS spectra obtained while applying V_p (1 V) and RF pulse trains with the indicated $f/2$ values (RF power of 1 dBm). Colour coded BLS intensity of (b)-(d) was normalised to the same value. (e) TR-BLS intensity integrated from 2.6 GHz to 3.5 GHz. The integration range (df) is illustrated by the horizontal line markers in (b)-(d). (f) Time dependence of V_p with (orange) and without (green) an added CW RF signal. (g) TR-BLS spectra measured while applying the voltage train only (RF off). (h)-(i) TR-BLS spectra obtained at two different $f/2$ values, within the injection-locking range (RF power of 1 dBm). Colour coded intensity of (g)-(i) are normalised to the same value. (j) Frequency-integrated TR-BLS signal showing the spin wave and the AO amplitudes at distinct time segments.

When the CW RF signal was switched on, at $f/2 = 2.8$ GHz, injection-locking is observed, as shown by the example TR-BLS spectra in Fig. 5(h), where the resulting AOs have larger amplitude compared to the natural AO signal. It is worth noting that the frequency upshift observed in Fig. 5(g) is suppressed due to injection-locking. Despite the improved frequency stability of the AO signal, no signal is detected in the time segments coincident with $V_p/2$.

Interestingly, when the frequency of the CW RF signal is larger than f_{AO}, as in the example shown in Fig. 5(i), a BLS signal is observed at $f/2 = 3.3$ GHz, in the time segments coincident with the $V_p/2$ level, while in the time segments coincident with the V_p level, the natural AO mode at f_{AO} is observed.

The observation of BLS signal in the time segments coincident with $V_p/2$ may be interpreted in the following

manner. While the pure spin current in the $V_p/2$ level may not be sufficient to fully compensate the damping and efficiently generate AOs, it still contributes to a decrease in the effective damping. In this scenario, a downshift of the spin wave band in the constriction region is expected, owing to partial damping compensation. As a consequence, when applying RF pulses with $f > f_{AO}$, one is able to directly excite and detect spin waves.

Figure 5(j) shows the TR-BLS signal integrated over a 450 MHz frequency range surrounding the spin wave the AO signal, as illustrated by the horizontal lines in Figs. 5(g)-(i). The data shows two TR-BLS signals corresponding to V_p and $V_p/2$, obtained at two distinct time segments of the duty cycle. These two signals differ in frequency by 0.5 GHz, as a result of the two different external RF frequencies and the natural AO frequency.

V. CONCLUSION

Using a single magnetic oscillator we generated nanosecond wide AO signals in the gigahertz frequency regime, under pulsed operation. We showed that a stable AO frequency in the time-domain can be achieved for certain optimal input voltage values, which tend to increase with decreasing pulse duration. The fact that we observed the response time of the circuit in the form of a time-varying AO frequency demonstrates that AOs can accompany the rapid changes in the instantaneous voltage of the input stimuli, at least within the nanosecond time-resolution of TR-BLS. The injection-locking experiments showed that the coupling of the SHNO to external microwave pulses results in improved temporal stability of the AO frequency and amplitude.

The control over the frequency response of magnetic oscillators plays an important role in applications. There exist a number of approaches via which the oscillation frequency can be controlled, for example, via changing the amplitude and polarity of the direct current[33] or the external magnetic field, injection-locking and voltage control [34]. Our results suggest that such approaches may also work efficiently under pulsed operation. Furthermore, we highlight that the tunability over the frequency and amplitude of magnetic oscillators, gained when combining pulsed voltage and injection-locking, can be viewed as a way to obtain frequency encoding and multi-level amplitude as outputs in the time-domain.

ACKNOWLEDGMENTS

Financial support by the Deutsche Forschungsgemeinschaft is gratefully acknowledged within program SCHU2922/1-1. Lithography was done at the Nanofabrication Facilities (NanoFaRo) at the Institute of Ion Beam Physics and Materials Research at HZDR.

[1] G. Csaba and W. Porod, Coupled oscillators for computing: A review and perspective, Applied Physics Reviews **7**, (2020).

[2] D. Marković, A. Mizrahi, D. Querlioz, and J. Grollier, Physics for neuromorphic computing, Nature Reviews Physics **2**, 499 (2020).

[3] J. Slonczewski, Current-driven excitation of magnetic multilayers, Journal of Magnetism and Magnetic Materials **159**, L1 (1996).

[4] L. Berger, Emission of spin waves by a magnetic multilayer traversed by a current, Phys. Rev. B **54**, 9353 (1996).

[5] A. Slavin and V. Tiberkevich, Nonlinear Auto-Oscillator Theory of Microwave Generation by Spin-Polarized Current, IEEE Transactions on Magnetics **45**, 1875 (2009).

[6] L. Liu, C.-F. Pai, D. C. Ralph, and R. A. Buhrman, Magnetic Oscillations Driven by the Spin Hall Effect in 3-Terminal Magnetic Tunnel Junction Devices, Physical Review Letters **109**, 186602 (2012).

[7] T. Chen, R. K. Dumas, A. Eklund, P. K. Muduli, A. Houshang, A. A. Awad, P. Dürrenfeld, B. G. Malm, A. Rusu, and J. Åkerman, Spin-torque and spin-hall nano-oscillators, Proceedings of the IEEE **104**, 1919 (2016).

[8] M. Dyakonov and V. Perel, Current-induced spin orientation of electrons in semiconductors, Physics Letters A **35**, 459 (1971).

[9] J. E. Hirsch, Spin hall effect, Phys. Rev. Lett. **83**, 1834 (1999).

[10] K. Ando, S. Takahashi, K. Harii, K. Sasage, J. Ieda, S. Maekawa, and E. Saitoh, Electric manipulation of spin relaxation using the spin hall effect, Physical Review Letters **101**, 1 (2008).

[11] A. Hoffmann, Spin hall effects in metals, IEEE Transactions on Magnetics **49**, 5172 (2013).

[12] J. Sinova, S. O. Valenzuela, J. Wunderlich, C. H. Back, and T. Jungwirth, Spin hall effects, Rev. Mod. Phys. **87**, 1213 (2015).

[13] V. E. Demidov, S. Urazhdin, A. Zholud, A. V. Sadovnikov, and S. O. Demokritov, Nanoconstriction-based spin-hall nano-oscillator, Applied Physics Letters **105**, 172410 (2014).

[14] B. Divinskiy, V. E. Demidov, S. Urazhdin, R. Freeman, A. B. Rinkevich, and S. O. Demokritov, Excitation and Amplification of Spin Waves by Spin-Orbit Torque, Advanced Materials **30**, 1802837 (2018).

[15] M. Dvornik, A. A. Awad, and J. Åkerman, Origin of Magnetization Auto-Oscillations in Constriction-Based Spin Hall Nano-Oscillators, Physical Review Applied **9**, 014017 (2018).

[16] S. Louis, O. Sulymenko, V. Tiberkevich, J. Li, D. Aloi, O. Prokopenko, I. Krivorotov, E. Bankowski, T. Meitzler, and A. Slavin, Ultra-fast wide band spectrum analyzer based on a rapidly tuned spin-torque nano-oscillator, Applied Physics Letters **113**, (2018).

[17] B. Dieny, I. L. Prejbeanu, K. Garello, P. Gambardella, P. Freitas, R. Lehndorff, W. Raberg, U. Ebels, S. O. Demokritov, J. Akerman, A. Deac, P. Pirro, C. Adel-

mann, A. Anane, A. V. Chumak, A. Hirohata, S. Mangin, S. O. Valenzuela, M. C. Onbaşlı, M. D'Aquino, G. Prenat, G. Finocchio, L. Lopez-Diaz, R. Chantrell, O. Chubykalo-Fesenko, and P. Bortolotti, Opportunities and challenges for spintronics in the microelectronics industry, Nature Electronics **3**, 446 (2020).

[18] S. Kaka, M. R. Pufall, W. H. Rippard, T. J. Silva, S. E. Russek, and J. A. Katine, Mutual phase-locking of microwave spin torque nano-oscillators, Nature **437**, 389 (2005).

[19] S. Sani, J. Persson, S. Mohseni, Y. Pogoryelov, P. Muduli, A. Eklund, G. Malm, M. Käll, A. Dmitriev, and J. Åkerman, Mutually synchronized bottom-up multi-nanocontact spin–torque oscillators, Nature Communications **4**, 2731 (2013).

[20] A. A. Awad, P. Dürrenfeld, A. Houshang, M. Dvornik, E. Iacocca, R. K. Dumas, and J. Åkerman, Long-range mutual synchronization of spin Hall nano-oscillators, Nature Physics **13**, 292 (2017).

[21] M. Romera, P. Talatchian, S. Tsunegi, F. Abreu Araujo, V. Cros, P. Bortolotti, J. Trastoy, K. Yakushiji, A. Fukushima, H. Kubota, S. Yuasa, M. Ernoult, D. Vodenicarevic, T. Hirtzlin, N. Locatelli, D. Querlioz, and J. Grollier, Vowel recognition with four coupled spin-torque nano-oscillators, Nature **563**, 230 (2018), arXiv:1711.02704.

[22] M. Zahedinejad, A. A. Awad, S. Muralidhar, R. Khymyn, H. Fulara, H. Mazraati, M. Dvornik, and J. Åkerman, Two-dimensional mutually synchronized spin Hall nano-oscillator arrays for neuromorphic computing, Nature Nanotechnology **15**, 47 (2020).

[23] J. Torrejon, M. Riou, F. A. Araujo, S. Tsunegi, G. Khalsa, D. Querlioz, P. Bortolotti, V. Cros, K. Yakushiji, A. Fukushima, H. Kubota, S. Yuasa, M. D. Stiles, and J. Grollier, Neuromorphic computing with nanoscale spintronic oscillators, Nature **547**, 428 (2017).

[24] M. Riou, F. Abreu Araujo, J. Torrejon, S. Tsunegi, G. Khalsa, D. Querlioz, P. Bortolotti, V. Cros, K. Yakushiji, A. Fukushima, H. Kubota, S. Yuasa, M. D. Stiles, and J. Grollier, Neuromorphic computing through time-multiplexing with a spin-torque nano-oscillator, Technical Digest - International Electron Devices Meeting, IEDM , 36.3.1 (2018).

[25] V. E. Demidov, H. Ulrichs, S. V. Gurevich, S. O. Demokritov, V. S. Tiberkevich, A. N. Slavin, A. Zholud, and S. Urazhdin, Synchronization of spin Hall nano-oscillators to external microwave signals, Nature Communications **5**, 3179 (2014).

[26] T. Hache, T. Weinhold, K. Schultheiss, J. Stigloher, F. Vilsmeier, C. Back, S. S. P. K. Arekapudi, O. Hellwig, J. Fassbender, and H. Schultheiss, Combined frequency and time domain measurements on injection-locked, constriction-based spin Hall nano-oscillators, Applied Physics Letters **114**, 102403 (2019).

[27] T. Sebastian, K. Schultheiss, B. Obry, B. Hillebrands, and H. Schultheiss, Micro-focused Brillouin light scattering: imaging spin waves at the nanoscale, Frontiers in Physics **3**, 1 (2015).

[28] The under(over)shoot values are likely underestimated since the circuit used for the voltage measurements shown in Fig. 1(c) only accounted the resistance-equivalent of the circuit under test (inductance and capacitance were not considered).

[29] Using an electrical detection method and while applying a direct current to drive the AOs under similar magnetic field conditions, we measured an AO linewidth of 20 MHz to 30 MHz.

[30] S. Urazhdin, V. Tiberkevich, and A. Slavin, Parametric excitation of a magnetic nanocontact by a microwave field, Physical Review Letters **105**, 1 (2010).

[31] E. Jué, M. R. Pufall, and W. H. Rippard, Asymmetric and partial injection locking of a three-terminal spin-torque oscillator, Applied Physics Letters **112**, (2018).

[32] K. Wagner, A. Smith, T. Hache, J.-R. Chen, L. Yang, E. Montoya, K. Schultheiss, J. Lindner, J. Fassbender, I. Krivorotov, and H. Schultheiss, Injection locking of multiple auto-oscillation modes in a tapered nanowire spin Hall oscillator, Scientific Reports **8**, 16040 (2018).

[33] T. Hache, M. Vaňatka, L. Flajšman, T. Weinhold, T. Hula, O. Ciubotariu, M. Albrecht, B. Arkook, I. Barsukov, L. Fallarino, O. Hellwig, J. Fassbender, M. Urbánek, and H. Schultheiss, Freestanding Positionable Microwave-Antenna Device for Magneto-Optical Spectroscopy Experiments, Physical Review Applied **13**, 054009 (2020).

[34] H. Fulara, M. Zahedinejad, R. Khymyn, M. Dvornik, S. Fukami, S. Kanai, H. Ohno, and J. Åkerman, Giant voltage-controlled modulation of spin Hall nano-oscillator damping, Nature Communications **11**, 4006 (2020).